Pack-boriding of Low Alloy Steel: Microstructure Evolution and Migration Behavior of Alloying Elements

Journal:	*Philosophical Magazine & Philosophical Magazine Letters*
Manuscript ID	TPHM-2019-0235.R1
Journal Selection:	Philosophical Magazine
Date Submitted by the Author:	23-Sep-2019
Complete List of Authors:	Litoria, Aditya; Indian Institute of Technology Indore, Metallurgy Engineering and Materials Science Figueroa, Carlos; Universidade de Caxias do Sul, PPGMATCentro de Ciências Exatas e Tecnologia Bim, Letícia; Universidade de Caxias do Sul, PPGMATCentro de Ciências Exatas e Tecnologia Pruncu, Catalin; Imperial College London, Mechanics of Materials Division, Department of Mechanical Engineering Joshi, Akshay; Bharat Forge Ltd, Kalyani Centre for Technology and Innovation Hosmani, Santosh; Indian Institute of Technology Indore, Metallurgy Engineering and Materials Science
Keywords:	borides, surface modification, EBSD, low-alloy steels, spectroscopy, kinetics
Keywords (user supplied):	EPMA, GDOES

Pack-boriding of Low Alloy Steel: Microstructure Evolution and Migration Behavior of Alloying Elements

A. K. Litoria[a], C. A. Figueroa[b], L. T. Bim[b], C. I. Pruncu[c], A. A. Joshi[d] and S. S. Hosmani[a]*

[a]*Discipline of Metallurgy Engineering and Materials Science, Indian Institute of Technology Indore, Khandwa Road, Simrol, Indore – 453552, India;* [b]*PPGMATCentro de Ciências Exatas e Tecnologia,Universidade de Caxias do Sul, 95070-560 Caxias do Sul, RS, Brazil;* [c]*Mechanics of Materials Division, Department of Mechanical Engineering, Imperial College London, South Kensington Campus, SW7 2AZ London, UK;* [d]*Kalyani Centre for Technology and Innovation (KCTI), Bharat Forge Ltd., Pune, India*

*** Corresponding author:**

Dr. Santosh S. Hosmani
Discipline of Metallurgy Engineering and Materials Science,
Indian Institute of Technology Indore,
Khandwa Road, Simrol, Indore – 453552, India
Email: sshosmani@iiti.ac.in; Phone: +91-7324306525

Email addresses of all authors:

Email: phd1701105009@iiti.ac.in (Aditya K. Litoria)

Email: sshosmani@iiti.ac.in (Santosh S. Hosmani)

Email: cafiguer@ucs.br (Carlos A. Figueroa)

Email: ltbim@ucs.br (Letícia T. Bim)

Email: c.pruncu@imperial.ac.uk (Catalin I. Pruncu)

Email: akshayjoshi13@gmail.com (Akshay A. Joshi)

Pack-boriding of Low Alloy Steel: Microstructure Evolution and Migration Behavior of Alloying Elements

Abstract -

Low alloy steel was pack-borided at different processing temperatures (at 850, 950, and 1050°C) and times (2, 4, and 6 h). The microstructural characterization of boronized steel showed the presence of three zones, namely boronized region containing finer grains and columnar geometry of $(Fe, M)_2B$ (where M = Cr, Mn, Mo, and Ni), transition zone, and non-boronized core. The concentrations of the alloying elements in $(Fe, M)_2B$ were increased from the surface to the core of the specimen. The pattern of slope variation of boron concentration-depth profile (obtained using GDOES) was linked with the boride morphology and process temperature. Pack-boriding of steel led to the development of systematic trend in slope variation of overall concentration-depth profiles of the alloying elements. The composition and morphology of boride affected the trend of slope variation for the boride-forming alloying elements. However, for Al and Si, the trend of slope variation was connected to the boride morphology and the composition of the matrix. Chemistry of the matrix was strongly dependent on the migration kinetics of the alloying elements during the boride growth. The migration kinetics of Cr, Mn, Mo, and C were found almost equivalent to the rate of boride growth. However, Ni, Al, and Si were migrated at a slower rate. Si showed the lowest migration kinetics among the alloying elements. The concentrations of the alloying elements having higher migration kinetics remained constant in the matrix during the boride growth.

Keywords: boride; boronizing; steel; surface alloying; GDOES; EPMA

1. Introduction

Pack-boriding has emerged as one of the most promising and effective surface modification routes to produce hard boride phases at the surface of the engineering alloys, enhancing its surface properties and thus, making it withstand against the surface degradation phenomenon such as wear, corrosion, and oxidation [1-3]. Boronizing, a thermo-chemical treatment, is accompanied by the controlled diffusion of boron into the metal surface producing different phases of metal borides (M-B, M = Fe, Cr, Ti, Ni, V, Mo, Mn, W, etc.) [4-14]. A considerable improvement in the quality of the surface layer is possible through combining the boronizing treatment with other surface treatments (like borocaburising, laser treatment on the boronized surface, etc.) [15, 16]. Boronizing is a proved lucrative option for many non-ferrous alloys [15, 17-19]. However, boronizing of ferrous alloys has got considerable attention due to their wide range of applications [20-22].

Typically, boronizing of iron-based alloys leads to the formation of iron-boride phases on the surface layer [15-17, 20-22]. The alloying chemistry has a significant influence on the boronizing behavior. The effect of various chemical elements on the boronizing response of pure iron was the subject of attraction in many kinds of literature [5-12]. The microstructure of the boronized layer, especially, the morphology of borides is dependent on the alloys, where the alloying elements can modify the solubility and diffusion of constituents [16, 23]. Low alloy steels show saw-tooth morphology of borides [20, 22, 24]. However, high alloy steels have an almost flat interface between the boride layer and substrate [21, 23]. Presence of W and V as alloying elements transforms the saw-tooth morphology into flat boride surface with smooth interfaces, along with the formation of transition zone that is rich in precipitates of W and V [10, 11]. There, the alloying elements can lead to the formation of a mixed boride phase in the layer.

The boronizing treatment of Fe-Cr alloy causes the formation (Fe, Cr)B phase at the top and (Fe, Cr)$_2$B phase beneath it [4]. The presence of Mo within the matrix promotes the precipitation of Mo_2FeB_2 in the boride layer [7, 8]. Gencer et al. obtained a boride layer containing FeB, Fe_2B, and precipitates of TiB_2 during boronizing of Fe-Ti alloy [12]. It was noted that the alloying elements could affect the kinetics, hardness, surface roughness, and tribological behavior of the boride layer [7, 8]. The thickness of the boride layer decreases due to the addition of alloying elements [10, 11]. Most of the archival literature has given a specific focus on the binary Fe-M alloys. However, the combined effect of the alloying elements on the boronized layer of steels is complex and least expounded. 34CrAlMo5-10 steel, popularly known as EN41B, belongs to the category of medium carbon low alloy steels containing C, Cr, Mn, Mo, Ni, Si, and Al as alloying elements. This steel is usually applied in valve stems, connecting rods, shackle pins and casting dies, etc. Understanding the effect of boron, multiple alloying elements, and processing parameters on the microstructure development and distribution kinetics of the alloying elements during the layer growth is one of the critical challenges. Consequently, the current work presents the effect of pack-boriding on the migration behavior of alloying elements in low alloy steel and the accompanying mechanism of microstructure development. Pack-borided specimens were investigated using optical microscopy, SEM, EBSD, XRD, EPMA, GDOES, and microhardness.

2. Experimental

A medium carbon low alloy steel (34CrAlMo5-10 / EN41B) with the following chemical composition was used: 0.4% C, 1.45% Cr, 0.57% Mn, 0.14% Mo, 0.11% Ni, 0.27% Si, 0.91% Al, 0.04% P, 0.04% S and balanced Fe. The specimens were cut and prepared in a square shape with dimensions 20 × 20 × 4 mm and ground up to 800 mesh size emery paper, followed by

diamond polishing and cleaning with acetone before boronizing. A preconditioned stainless-steel container was used to boronize the specimens at 850, 950, and 1050°C for 2, 4, and 6 h using the commercially available Boropak™ powder (typically, the commercially available boronizing powder contains about 5% B_4C as a source of boron + 5% KBF_4 as an activator + 90% SiC as a diluent). The specimens were embedded inside the powder bed at the center of a container. The top portion of the container was covered with SiC powder. The detailed boronizing process is mentioned elsewhere [20]. The container was air-cooled after boronizing.

Cross-section of boronized specimens was metallographically prepared and etched using 2% Nital. The microstructural investigations were performed using an optical microscope (Make: Zeiss Axio Vert.A1), scanning electron microscopy (SEM, Make: Zeiss Supra55), X-ray diffraction (XRD, Make: Bruker D2-Phaser), and microhardness tester (Make: Walter UHL VMH-002). XRD patterns were recorded using Cu-Kα radiation.

In order to obtain the grain structural morphology of the specimen boronized at 1050°C for 4 h, cross-section was prepared using different grit paper (starting from 800 to 4000). Final polishing was done using the diamond suspension (1 μm for 8 min) and a standard colloidal silica suspension (0.4 μm for 25 min). The prepared specimen was observed for the microstructure by a Hitachi 3400 SEM, which contains a Bruker e-flash electron-backscatter-diffraction (EBSD) detector. The followings parameters were used during the measurements: 20 kV acceleration voltage, 10 mA current density, and the step size of ~1 μm. The acquired images were post-processed using ATEX [25] and MTEX software.

Elemental composition of the boronized layer was determined using electron probe microanalysis (EPMA). EPMA measurements were done using a JEOL JXA-8530F instrument having 3 WDS and 1 EDS channels. The accelerating voltage and the beam current were settled

as 15 kV and 50 nA, respectively. Line scan was carried out within the boride column and the adjacent non-boride region. Elemental mapping was performed in the boronized layer to understand the distribution of B, Fe, Al, Cr, and Mo. Each map covers the area of 140 μm × 180 μm. The measurements were taken under an acceleration voltage of 15 kV, beam current of 50 nA, dwell time of 10 ms/point at the intervals of 0.5 μm.

Boronized specimens were further analyzed using glow discharge optical emission spectroscopy (GDOES, Make: Horiba GD Profiler 2). Semi-quantitative depth profiles of B, Fe, Cr, Mn, Mo, Ni, Si, and Al were obtained using GDOES. This technique allows to observe the surface ejection of atoms in the excited state, which is detected due to optical emission after decaying to the fundamental state by photoelectric sensors for specific wavelength [26].

3. Results and Discussion

3.1. Phase Analysis, Microstructure, and Hardness

Figure 1 shows the x-ray diffractograms (XRD) of boronized specimens at different temperatures. The untreated specimen shows the diffracted peaks of ferrite (α-Fe). It was noticed the characteristic diffraction pattern of Fe_2B present in all boronized specimens. However, the specimen boronized at 1050°C showed additional small peaks of FeB and SiC. The presence of both iron-borides (FeB and Fe_2B) indicates that the FeB phase may be formed only in some places on the specimen surface. Therefore, the phase maps shown in Fig. 3(c)-(d) and the micrograph incorporated in the later portion of Section 3 do not show the distinct layer or evidence of FeB (Fig. 9(d)). Evaporation of boron oxides plays a vital role in controlling the supply of boron for its reaction with the steel surface during powder-pack boriding using B_4C as a boron source [16]. Therefore, the high temperate can lead to a high boron potential with the pack-mixture leading to the formation of FeB [16, 20, 21]. When is used high boronizing

temperature, the sticky/diffused layer of boronizing pack-mixture (which contains SiC) is relatively difficult to remove by cleaning, and therefore, XRD shows SiC peaks at 1050°C.

Figure 2(a) and (b) shows the microstructure in cross-section of the specimen boronized at 950°C for 4 h. One can see a columnar morphology of iron-borides in the modified region. The prominent anisotropy of the diffusion coefficient in the tetragonal lattice of Fe_2B may is responsible for the formation of columnar morphology [14, 23, 27]. The SEM micrograph shows microstructural features that are difficult to be seen in the optical micrograph (Fig. 2(a) versus (b)). The boride columns that appear thick in the optical micrographs are formed by clustering thin columns.

A cross-sectional micrograph with the SEM analysis of pack-borided steel is presented in Fig. 3(a). This reveals the formation of boride region, which is darker in respect to the non-boronized core. Preferentially oriented grains in the surface region of the boronized cross-section are observed in the IPF map, as shown in Fig. 3(b). These grains are Fe_2B columns, formed through the diffusion of boron atoms [28], which were noted to grow perpendicular to the surface in a needle-like manner [29]. FeB is not considered due to the detection of its poor signals. The IPF map shows that the Fe_2B grains are mostly oriented around {100} and {110} (Fig. 3(b)). Figure 3(e) shows the strong texture of Fe_2B grains toward the horizontal extremities. Iron-boride prefers to grow in the crystallographic direction [001] and by stacking crystal planes {001} [27]. Texture in the Fe_2B phase could occur due to the mutual compression between adjacent grains and the lattice mismatch between the phases [27]. Small grains of Fe_2B are formed near the surface (Fig. 3(c)-(d)). Random orientation of grains is visible in the area beneath the boronized region (Fig. 3 (b)).

Boronized region consists of iron-boride phase and is surrounded by non-borided matrix. The matrix shows a different contrast in the optical micrograph (Fig. 2(a) and Fig. 3) compared to the underneath regions. Tiny particles are apparent in the matrix and on the front of boride columns. These tiny boride particles are generally present at high-angle prior-austenitic grain boundaries [4].

The 'transition zone' is labelled in the vicinity of boronized region that contains boride particles in the non-transformed areas (see the subsequent sections for more details). The total boronized layer is divided into the boronized region and the transition zone [20]. The non-boronized core follows the transition zone.

Figure 2(c) shows the microhardness-depth profiles for the specimens boronized at 850, 950, and 1050°C for 4 h. The hardness measurements near to the surface (within ~20 μm) are not representative for the real mechanical behavior; thus, the hardness is recorded after 20 μm. Maximum hardness of about 1050, 1500, and 1800 $HV_{0.1}$ are detected in the near-surface region at 850, 950, and 1050°C, respectively. There, it is possible to obtain a constant hardness in the boronized region if the iron-boride columns occupy the entire space of the region [1]. However, the observed decrease in the hardness from the near-surface area to the core (Fig. 2(c)) is due to the increase in the proportion of non-borided matrix surrounding the iron-boride columns [5, 20, 30]. Compositional analysis of the specimens borided at 850°C (Section 3.3) confirmed that boride fraction in the surface region is less than one (i.e., the surface region is not occupied entirely by the boride phase). Therefore, the lower surface hardness at 850°C is due to the presence of softer non-boride regions surrounding the boride phase. At any depth within the boronized layer, the reduced hardness for lower temperature is due to the smaller fraction of iron-boride.

3.2. Compositional Analysis: EPMA

Figure 4 shows the BSE image and the corresponding EPMA measurements from surface to non-boronized region of the specimen boronized at 950°C for 4 h. The iron-boride phase appears gray colored in the BSE micrograph (Fig. 4(a)) because of the significant presence of boron (light element) [1, 20]. Porosities are distinguishable in BSE mode due to their black appearance. One can see that the region with iron-boride shows the highest boron concentration. From here, the 'depth' term refers to the distance from the surface up to a certain point in the bulk. The concentration of the alloying elements is lower in the boride than the non-borided core. The much lower content of Si and Al in the boride than the non-boronized area suggests that the growing boride significantly rejects Si and Al atoms [31]. The elemental mapping of Al in Fig. 5(d) shows more concentration of Al in front/surrounding regions of the boride column than the non-boronized region. The relevant GDOES results are discussed later. The fluctuation in the elemental concentration-depth profiles is possible due to the presence of boundaries/gaps between the clustered thin boride columns at the location of EPMA measurements.

The concentrations of alloying elements, except Si, Al, and C (see also the subsequent section), never reaches zero in the boride phase (Fig. 4). The concentrations of Cr, Mn, Mo, and Ni show an increasing trend from the surface to the tip of the boride column, which is possible due to the redistribution of the alloying elements (boride has different solubilities for different elements) and nonequilibrium conditions that prevail during the growth of boronized layer [1, 23]. A similar trend in the distribution of alloying elements is evident for the boronized Fe-Cr [1] and Fe-Mn [5, 6] alloys. The presence of Si and Al in the boronized region at the location of EPMA measurements, especially, near to the surface is associated with their

segregation/entrapment between the growing boride columns (see the regions indicated by arrows in Fig. 5(d)). Boride formed near to the surface could assimilate some Si from the boronizing pack-mixture, which contains SiC powder [20].

Figure 5(b)-(f) shows the elemental mapping of vital elements in the boronized region and some portion of the transition zone of the specimens boronized at 950°C for 4 h. The B and Fe distributions confirm the presence of columnar iron boride in the boronized region due to both chemical signals that follow quite well the morphology previously observed in the SEM micrographs. In the elemental mapping, the near-surface region of the layer does not indicate the formation of a higher B contained generally by the iron-boride (FeB) phase. Therefore, it agrees with the XRD results shown in Fig. 1. Boride columns appear dark in the Al mapping. Al enriches the regions between the boride columns and the growing front of the borides. These results confirm that Al does not dissolve in the boride phase, and it is displaced away during phase growth [31]. Unlike the mappings of B, Fe, and Al, the Cr and Mo mappings do not show a clear distinction between the boride columns and the surrounding non-boride region, which is due to the presence of Cr and Mo in both the boride phase and non-boride region [1, 7]. However, the Cr mapping shows dark patches within the boronized region. These patches are mostly the narrow regions between the iron-boride columns, which are occupied by the boride during subsequent growth. For better understanding, Fig. 5(d) and (e) shows the encircled such regions between the iron-boride columns. The darker appearance indicates the Cr depletion. However, it should be remembered that the iron-boride columns do not absorb the entire concentration of the element present in the alloy (Fig. 4). Hence, some rejection occurs during the growth of boride [23]. Therefore, Cr depletion in the narrow regions between the boride columns hints the faster migration of Cr than the growth kinetics of the iron-boride columns.

Some of the regions indicated by arrows in Fig. 5 (as an example, Fe and Al mappings) reveal the presence of small non-borided areas trapped between the columns. Open zones are also observed between the boride columns (Fig. 5(a)). Based on the above observations, the boride phase contains Fe and B with some concentration of Cr, Mn, Ni and Mo, i.e., the boride formed is $(Fe, M)_2B$ where, M = Cr, Mn, Mo, and Ni [4-7, 21, 23]. The concentration of the alloying elements in the boride column decreases from the core to surface. In the text, Fe_2B designates $(Fe, M)_2B$ for conciseness. Formations of separate borides of alloying elements (like Cr_2B or MnB_2) in the Fe_2B columns are ruled out because of the low concentrations of the alloying elements in the investigated steel [1, 5].

3.3. Compositional Analysis: GDOES

Unlike the EPMA results, shown in Fig. 4, a gradual decrease in the concentration of B, and some rise in the concentrations of the remaining elements (Fe, Cr, Mn, Ni, Mo, Si, and Al) from the surface to the non-boronized region are observed in GDOES results (Fig. 6). This difference is ascribed to the fact that the EPMA measurements are done within the boride column (Fig. 4). However, GDOES gives the results at various depths from a considerably large area (diameter of the crater is ~ 4 mm). Therefore, the obtained results from each depth within the boronized region are the average concentration of the boride phase and the surrounding non-boride area [23]. As an example, the EPMA concentration-depth profile and elemental mapping confirm the absence of Al in the boride, while the concentration of Al in the surrounding regions of boride is higher than the transition zone and core. Therefore, the decreasing trend of Al content from zone-V to I in GDOES (Fig. 6) is a direct consequence of depleted proportion of non-boride regions towards the surface.

GDOES results (Fig. 6) show the presence of 5 compositional zones (I to V) in the boronized region. These zones are identified based on the change in slopes (the first derivate of concentration function versus depth or rate of change of concentration versus depth) of GDOES profiles with the distance from the surface or core (Fig. 7). Most of the alloying elements achieve stability in zone-I. Si and Al contents show a noticeable drop during the transition from zone-II to I. Al content become almost zero in the zone-I. The Si content above zero in the zone-I is possible due to its absorption from the surrounding pack-mixture [20]. The plateau in the concentration profiles of boron (subsequent discussion explains the absence of plateau in boron profile at 850°C) in the zone-I indicate the formation of vastly boride phase and a negligible quantity of non-boride region near to the surface at 950°C. The B and Fe rich regions attempt to wipe the other alloying elements during the growth [23]. The extent of migration of alloying elements is one of the factors controlling the overall concentration of alloying elements at various depths. The growth kinetics of boride columns regulates the extent of wiping [22, 23]. In the process of boride formation, the iron-boride phase partially dissolves some of the alloying elements (like Cr, Mn, Ni, and Mo) and entirely discards the other alloying elements (like C, Si, and Al) [31]. GDOES results of the boronized Ti-alloy also showed the rejection of Al by the growing boride [32]. In the transition zone-V, the sharpest drop in the concentration of B with the increase of depth is associated with the steepest rise in the concentration of all elements, except Si and Al. Finally, zone-V shows the accumulation of Si and Al.

The variation trend of slopes for concentration-depth profiles of alloying elements at 850°C is analogous to that of the specimen boronized at 950°C (Figs. 6(b) and 7(b)). Even if the concentration-depth profile of B is steeper and variation in the slope with depth is not discerned at 850°C, some similarity in its trend is noticeable in zones-III to V (Fig. 7). Variation in the

slope of B profile becomes distinct as the boronizing temperature increases to 950°C. The slope change in the concentration-depth profiles of all elements, except C, is observed in different zones. In contrast to the other alloying elements, C content in zones-I to IV is absent at 950°C. At lower temperature (850°C), carbon is not found in zone-I to III. The entire absence of C in these zones indicates its faster migration away from the boronized region at both temperatures [23]. Another reason for the lack of C could be its insolubility in the Al- and Si- rich matrix. Accumulated Al and Si can form the complex compound in the matrix surrounding the boride columns [31].

A sequence of the events occurred during the growth of the boronized region is resembled to the course of development of zones from V to I. It is because, the journey of layer growth starts with a non-boronized core (i.e., the deeper region near to zone-V) to the layer of fully occupied boride phase (i.e., zone-I). Therefore, the subsequent discussion explains the events occurring from core to surface. As mentioned above, the slope of the GDOES profiles varies systematically, and the pattern for the alloying elements is almost identical at 950°C and 850°C (Fig. 7). The steeper slope is followed by, the shallower slope and vice-versa. The increasing slope of all elements (either in the positive or negative direction) approaches towards the zero and then, increases again. The pattern of slope change for Cr, Mn, and Mo profiles is like a mirror image of the slope profile of B at 950°C. The sequence of slope variation in different zones is identical for Si and Al. Moving from zone-V towards the surface, as the slopes of B, Cr, Mn, Mo and Ni profiles approach towards zero (at the interface of zones-IV and III), the slopes of Si and Al profiles move away from zero and reach the maximum either at the interface of zones-IV and III (for 950°C) or in zone-III (for 850°C). However, the slopes of all elements approach to zero and achieve better stability while moving in the zones-II and I. The

complete transformation of the surface region to boride causes the slight increase in the composition (i.e., negative slope) of Cr, Mn, and Mo in zone-I. The slope of B profile becomes positive in zone-I (i.e., B concentration decreases near to the surface) at 950°C, which is possible due to the formation of macro-defects, like porosities [3, 6], in the near-surface region. Segregation of Ni occurs at the interface of zones-I and II, which is also evident at the lower boronizing temperature of 850°C. However, EPMA measurements within the boride column do not manifest such segregation in the near-surface region suggesting that during the transformation of the entire extension of the surface to the boride phase, some fraction of Ni atoms are discarded in the surrounding matrix retaining some in the boride phase.

Even if the trend in the variation of slopes for alloying elements at 850°C is almost comparable to that of at 950°C, the position of the slope peaks concerning each other in different zones is not identical at both temperatures (Fig. 7). The slope profiles show a backward shift in the peak positions at 850°C. For example, the locations of the peaks for Cr, Mn, Mo, and Ni, concerning the position of peaks for Si and Al at the interface of zones-V and IV, are shifted towards the leftward at 850°C. This observation confirms the role of temperature on the growth behaviour of boride and the compositional adjustments between boride and its surrounding matrix. It also reflects the difference in migration kinetics among alloying elements during the boronizing process.

The depth corresponding to the maximum accumulation in zone-V (i.e., the intersection of slope profiles to X-axis at Y = 0) is lower for Si than Al. The peaks positions in the slope profiles are at lower depths for Si than Al (however, the difference in the peak positions of Si and Al is smaller at 950°C than 850°C). These signals suggest slower migration kinetics of Si than Al.

For Ni, the position of the first peak while moving from zone-V to I occurs at a considerably lower depth than that for Cr, Mn, and Mo. It indicates the absence of Ni migration even though the other alloying elements start depleting (during the formation of boride particles). This situation is possible due to the lower migration kinetics of Ni than Cr, Mn, and Mo. Positions of peaks for Cr, Mn, and Mo are almost at the same depth that demonstrates the inconsequential difference in their migration kinetics.

Figure 8 shows the normalized concentration-depth profiles of B and their corresponding slope variations for the specimens boronized at 850, 950, and 1050°C for 4 h. The thickness of the layer increases with temperature. For the relative comparison of these concentration-depth profiles at different temperatures, they are normalized by making the maximum B concentration in Fe_2B layer as the unity. A considerable jump in B content near to the surface at 1050°C is possibly due to the presence of FeB phase, as detected by XRD (Fig. 1), at some locations on the surface. Unlike 850 and 950°C, the increasing concentration of B from the core to surface is very gradual at 1050°C, and the slope of the profile approaches towards almost zero at the 50% of the boronized layer thickness (thickness of boronized region plus transition zone). This gradual change indicates the presence of unreacted Fe in the broader transition zone. Tiny particles of boride are apparent in areas close to the core and surrounding the boride columns (Fig. 9 and Fig. 2(b)). The equilibrium solubility product (K) of the boride controls the extent of the transition zone [33]. Typically, K increases with temperature [33, 34]. Therefore, the tendency for dissolution of boride at higher temperature causes a broader transition zone.

Typically, the growth of boride is faster in the forward direction than the transverse direction causing a columnar morphology (i.e., a sharp change in the average width or volume of boride) [23, 24] and therefore, an abrupt change in boron profile is expected in this case.

However, at 1050°C, a gradual change in B profile from the surface to the steel core is possible. It is due to the higher rate of nucleation and growth of boride particles in the matrix [4] or accelerated growth of boride columns in the transverse direction as compared to the forwarding direction. Hence, variation in the slope of B profile is a direct indication of boride morphology. Moreover, a slope change in the B profiles on different zones indicates a non-uniformity in the growth kinetics of boride columns. The extent of region (above the transition zone) having the slope of B profile, d(B)/dx, close to zero is considerably broader at 1050°C than that of at 950°C (see inserts in Fig. 8(b)). It may indicate the constant boride fraction (f_B) in this region. At the interface of zones-III and IV (Fig. 6(a)), for the same value of B on either side, Si and Al contents are lower in zone-III than zone-IV that suggests the possible role of reducing their accumulation for further growth of boride.

Figure 9 shows the change in the appearance of boride morphology with temperature. Tips of the boride columns show considerable thickening (or blunting) and branching at 1050°C leading to the decrease in gaps between the columns. In contrast, the boride columns are relatively narrow and have sharp tips at 850°C. In case of 950°C, the tips of boride columns are sharper than that of at 1050°C and show more thickening towards the surface than at 850°C. These boride morphologies support the trend in variation of B content (and hence, f_B) with depth in the boronized layer. The continuous rise in the B content even in zone-I at 850°C indicates that f_B is possibly close to 1, but not equal to 1. The boride growth kinetics is concurrent with the change in slopes of the concentration-depth profiles of other alloying elements.

3.4. Effect of Process Time

Figures 10 and 11 show the concentration-depth profiles of various elements and their slopes (rate of change), respectively, of specimens boronized at 950°C for different process times. The trend in the variation of slopes is similar to the Figs. 6 and 7. Peaks designated as p1 in Fig. 11 correspond to depths at (i) the sharp drop in the concentration of alloying elements (i.e., the maximum slope in the positive direction), and (ii) the sharp rise in B content (i.e., the maximum slope in the negative direction) while moving from core to surface. Peaks labelled as p2 correspond to the accumulation of Al and Si towards the core. For Al and Si, Al-2 and Si-2 designate the depths at p1, and Al-1 and Si-1 assign the depths at p2. Fig. 12(a) shows the depths corresponding to p1 and p2 for the elements present in the boronized steel. The horizontal dashed lines indicate the depths for B. As a general observation, the depths for Ni, Al, and Si are lower than that of B. For example, Fig. 12(b) compares the profiles of B and Ni, where the depth that corresponds to the beginning in the drop of Ni content is leftward to the depth corresponding to the start in rising of B content. Al-1 and Si-1 are nearer to the depth for B as compare to Al-2 and Si-2, which suggests that the system prefers accumulation of Al and Si over the depletion during the boride formation.

Typically, in the surface alloying process, the square of the depth is proportional to the duration of the process. There, the proportionality constant indicates the rate of events occurring during the process [1, 23]. The coefficient of determination (R^2) for a linear regression of the square of depths for the elements (Fig. 12(a)) with time is 0.94 ± 0.04. The slope of the linear regression line for boron indicates the boride growth rate. However, the slopes corresponding to other alloying elements show their migration kinetics during the boride growth. Figure 12(c) shows such determined rates of the events.

Figure 12(c) shows that Cr, Mn, Mo, and C migrate at slightly higher rate than the rate of boride growth causing the lower tendency of these elements to accumulate (in the non-boride areas surrounding the boride columns: see Fig. 5(e)-(f)) [1, 5, 6, 23]. However, Ni, Al, and Si migrate at a slower rate than Cr, Mn, Mo, and C. The kinetics of migration of Al and Si that cause the accumulation in the transition zone (near the core) is faster than the rate determined at Al-2 and Si-2. The lower migration kinetics of Al and Si in the matrix than in the transition zone caused the higher concentration of these elements in the matrix than the transition zone (for example, see Fig. 5(d)).

At the locations of Al-2 and Si-2, the slope of the B profile is approached to zero (i.e., stagnation in the boride growth: see Figs. 7 and 11). Therefore, f_B is constant at those locations, and the decreased accumulation in the matrix should be responsible for the sharp depletions in the overall concentrations of Al and Si at Al-2 and Si-2 locations, respectively. Concentrations of the alloying elements affect the growth kinetics of borides [7, 9]. The lower migration kinetics of Al and Si at the locations where stagnation in the boride growth occurs suggest that the reduction in accumulation in the matrix is required to overcome the stagnation and, hence, to generate a further growth of boride.

3.5. Theoretical Interpretation of EPMA and GDOES Results

The discussion mentioned in the previous sections is further apprehended as follows. Due to the columnar morphology of iron-boride, GDOES measures the composition of boride and the surrounding non-boride regions (matrix) at every depth. Therefore, the trend in the concentration-depth profiles of various elements (Fig. 6) and their slopes (Fig. 7) are directly associated with the variation in compositions and proportions of boride and matrix. Assume, *i* is

the alloying element in the steel, which is further subclassified as *i-B* (element present in boride (i.e., Cr, Mn, Mo, and Ni)) and *i-NB* (element absent in boride (i.e., Si and Al)). The carbon is excluded because of its absence in the pack-borided surface region. It is considered, the concentrations of alloying element *i* at depth *j* in the boride phase and the matrix are $c_B^{i,j}$ and $c_m^{i,j}$, respectively (here, *i* can be *i-B* or *i-NB*). If f_B and f_m are the fractions (concerning weight or volume) of boride and matrix respectively, $f_B + f_m = 1$. The total composition of *i* at depth *j* is given by,

$$c_t^{i,j} = c_B^{i,j} \cdot f_B + c_m^{i,j} \cdot f_m \quad (1)$$

EPMA (Fig. 4) and GDOES results (Fig. 6) have confirmed that the boride phase contains a lower concentration of the alloying elements than the matrix. Let assume, $\Delta c^{i,j}$ is the difference in the composition of matrix and boride, i.e., $\Delta c^{i,j} = c_m^{i,j} - c_B^{i,j}$. Therefore,

$$c_t^{i,j} = \left(c_m^{i,j} - \Delta c^{i,j}\right) \cdot f_B + c_m^{i,j} \cdot f_m \quad (2)$$

which, further is simplified as

$$c_t^{i,j} = c_m^{i,j} - \left(\Delta c^{i,j} \cdot f_B\right). \quad (3)$$

In the case of *i-B*, $\Delta c^{i-B,j}$ has a positive value, and it increases from the core to surface. However, in the case of *i-NB*, $c_B^{i-NB,j} \approx 0$ (confirmed by EPMA and GDOES results). Hence,

$$c_t^{i-NB,j} = c_m^{i-NB,j} \cdot f_m. \quad (4)$$

As established in the previous section, the migration rate of *i*-B is almost close to the rate of boride growth, which indicates that the rejection of *i-B* by the growing boride and its migration in the matrix strike at the same rate. Therefore, $c_m^{i-B,j}$ remains constant during the boride growth (as a confirmation, varying contents of the elements in the matrix is not evident in Fig. 5(e)-(f)).

In zone-II, *i-NB* has almost horizontal concentration-depth profiles (i.e., slope = 0) with an increased f_B (or decreased f_m). A considerable increase in $c_m^{i-NB,j}$ (see Eq. (4)) is required to maintain this situation. Figure 5(d) confirms this by showing the higher concentration of Al in the matrix. Accumulation in the matrix indicates that the rejected *i-NB* diffuse away from the growing boride front at a slower rate causing $c_m^{i-NB,j}$ as a variable during the boride growth.

Concisely, the trend of alternate steeper and shallower slopes of $c_t^{i-B,j}$ profiles are related to the variation in f_B and $c_B^{i-NB,j}$ (Eq. (3) and constant $c_m^{i-B,j}$). In other word, profiles of $c_t^{i-B,j}$ are mainly dependent on the composition and morphology of boride, which explains why the Cr, Mn, and Mo profiles appear like the mirror images of the B profiles (Figs. 6, 7, 10, and 11). However, the pattern of variation in the slopes of the $c_t^{i-NB,j}$ profiles are associated with the changes in the morphology of boride (linked to f_B) and chemical structure of matrix ($c_m^{i-NB,j}$) (Eq. (4)). Here, the morphology of boride is a common factor in controlling the trends in $c_t^{i-B,j}$ and $c_t^{i-NB,j}$ profiles.

3.6. Mechanism

The obtained results indicate the occurrence of the following events during pack-boriding of the 34CrAlMo5-10 low alloy steel surface.

In the boriding pack-mixture, activator (KBF_4) generates boron halide gases (like BF_3), which (along with O_2 trapped in the boriding mixture) reacts with the source of boron (B_4C) and diluent (SiC), and generate a favorable atmosphere for the boronizing of steel through the following reaction [16, 20, 22, 35]:

$$B_4C + 3SiC + 3O_2 \xrightarrow{BF_3,\ SiF_4} 4B + 2Si + SiO_2 + 4CO \qquad (5)$$

Like the other surface alloying techniques [36, 37], boron enters the steel surface (B → [B]) due to its high chemical potential in the surrounding pack-mixture, and then, achieves a steady-state. The dissolved boron at surface reacts with the elements (M) present in the steel through the reaction (6):

$$[B] + 2M \rightarrow M_2B \quad (6)$$

Initially, boride starts nucleating at the high-angle austenitic grain boundaries [4] and multiple locations on the surface (Fig. 13(a)). The nucleating and growing boride particles discard alloying elements because the boride has low or no solubility as most of the alloying elements present in the steel (Figs. 4-6) [4-13]. Boride has the lower solubility (as compared to the non-boride region or core) for Cr, Mn, Mo and Ni, and almost zero solubility for C, Si, and Al. The overall content of the elements at any depth within the boronized layer depends on the composition and proportions of boride and matrix. Due to the formation of iron-boride, B content increases sharply during the initial stages causing the sharp decrease in the overall content of Cr, Mn, Mo, and Ni without much change in their concentration in the matrix. Here, a delay in the reduction of Ni content is possible due to its lower migration kinetics. However, the overall content of Si and Al increases with increasing B content due to the sharp increase in their concentration in the matrix. Figure 13 shows the difference in composition of matrix region (surrounding the boride) and the core using the gray and white colors, respectively. Accumulation of Al occurs before Si. Initial boride formation leads to a significant reduction of C content, which is finally displaced away from the borides [23]. However, further formation of boride particles leads to increase in the C content to some extent (due to the sudden rise in the supply of rejected carbon by the growing boride particles) and subsequently, sharp depletion to almost zero content [23]. Rejected C in front of the growing boride can form cementite (Fe_3C) or

borocarbides ($Fe_3(B,C)$) in the transition zone [4, 16, 20, 38]. The following sequence of migration kinetics (MK_i) of the alloying elements, i, causes these differences in their response during the growth of boride: $MK_{Cr/Mn/Mo/C} > MK_{Ni} > MK_{Al} > MK_{Si}$. The region containing boride particles and the matrix containing the accumulated or rejected (by boride) alloying elements is called the transition zone. A higher temperature increases the extent of the transition zone (Figs. 8 and 9). The matrix region (grey shaded regions shown in the schematic diagrams in Fig. 13) could penetrate/extend in the transition zone at high boronizing temperature (Fig. 9(d)). Composition of boride and matrix changes continuously as the boronizing process progresses. The growth of already nucleated borides in the forwarding direction gives them a columnar morphology ([001]. It corresponds to a maximum atomic density of B and is the most natural path for the diffusion of B in Fe_2B [24]). In parallel, new boride particles nucleate in the transition zone (which later become a part of the growing boride columns) (Fig. 13(b)-(e)). During this growth, the concentration of Si and Al in boride remains almost zero, and their accumulation in the matrix decreases to some extent (to accelerate the boride growth) and then, increases again at a later stage (due to the mismatch between rejection rate and migration kinetics of the elements). The extent of the region accumulated with Si and Al increases during further growth. The concentration of Cr, Mn, Mo, and Ni in iron-boride decreases without changing their content in the matrix (because the rejection and migration of these elements occur at the same rate) during the growth of boronized region. During the transformation of the entire region to boride (f_B = 1) near to the surface, the concentration of the alloying elements in boride could increase slightly (possibly, to accommodate the change in equilibrium situation from two phases to a single phase). Porosities could form at the interface of boride columns (especially, near to the surface) due to the persistent exposure of the specimen surface at the generated gases

and oxygen in the pack-mixture [2, 6]. The porosities could increase with boronizing temperature (Fig. 9) [6]. Due to the continuous supply of boron from the surface, the boundaries of the boride grains at the fully transformed surface can act as the nucleation sites for the formation of small grains of the boride (Fig. 3).

4. Conclusions

1) Pack-boriding of 34CrAlMo5-10 (EN41B) steel revealed the presence of mainly (Fe, M)$_2$B layer, where M = Cr, Mn, Mo, and Ni. The concentrations of the alloying elements in (Fe, M)$_2$B were increased from the surface to core. The solubilities of C, Al, and Si were found almost zero in iron-boride phase.
2) The microstructure in the cross-section of boronized specimens, starting from the surface to core, showed the presence of (i) small grains of iron-boride near the surface, (ii) columnar iron-boride and the surrounding non-boride region (called as 'matrix'), (iii) transition zone that contains tiny boride particles in the non-transformed areas, and (iv) non-boronized core. The morphology of iron-boride and extent of the transition zone were dependent on the temperature. IPF map showed that the columnar grains of Fe_2B were oriented mostly around {100} and {110}. The strong texture of Fe_2B grains was observed in [001] crystallographic direction. Maximum hardness of about 1050, 1500, and 1800 $HV_{0.1}$ were detected in the near-surface region at 850, 950, and 1050°C, respectively.
3) EPMA and GDOES prove to be promising tools to elucidate the boride growth behavior. The trend of variation in the slope of the boron concentration-depth profile was linked with the boride morphology and process temperature. Concentration-depth profile of

boron was steeper, and the change in its slope with depth was not discerned at 850°C. However, the variation in the slope of the boron profile became distinct at higher process temperature.

4) Pack-boriding of steel led to the formation of a systematic trend in the slope variation of overall concentration-depth profiles of the alloying elements. The steeper slope was followed by, the shallower slope and vice-versa. The pattern of change in the slopes of the boride forming alloying elements was connected to the composition and morphology of boride. However, for Al and Si, it was related to the boride morphology and the composition of the matrix.

5) The chemical composition of the matrix was dependent on the solubility and migration kinetics of the alloying elements. The migration kinetics of the alloying elements and the rate of boride growth were interlinked. The migration kinetics of Cr, Mn, Mo, and C were almost equivalent to the rate of boride growth. However, Ni, Al, and Si were migrated at slower rates. Si showed the lowest migration kinetics among the alloying elements. The migration kinetics of Al and Si was lower in the matrix than in the transition zone, which caused the higher concentration of these elements in the matrix than the transition zone. Carbon was entirely missing in the boronized region. The concentrations of the alloying elements having higher migration kinetics remained constant in the matrix during the boride growth.

Acknowledgments:

AKL thanks IIT Indore (IITI) for providing scholarship to do Ph.D. research. GDOES measurements were partially financed by Grant CNPq-INCT-INES # 465423/2014-0. CAF is a CNPq fellow. Authors acknowledge Dr. Jun Jiang (Imperial College London, UK) for supporting the EBSD measurements. Authors thank Sophisticated Instrument Centre, IITI and Central Facility of Materials Engineering, IISc Bengaluru for characterizations. Authors appreciate Dr. Rupesh S. Devan (IITI) for useful discussions and proofreading the manuscript.

References:

[1] V.I. Dybkov, L.V. Goncharuk, V.G. Khoruzha, A.V. Samelyuk, and V.R. Sidorko, *Growth kinetics and abrasive wear resistance of boride layers on the Fe-15Cr alloy*, Mater. Sci. Technol. 27 (2011), pp. 1502-1512.

[2] E. Dokumaci, I. Ozkan, and B. Onay, *Effect of boronizing on the cyclic oxidation of stainless steel*, Surf. Coat. Technol. 232 (2013), pp. 22–25.

[3] H. Wang, Y. Zhao, X. Yuan, K. Chen, and R. Xu, *Effects of boronizing treatment on corrosion resistance of 65Mn steel in two acid mediums*, Phys. Procedia. 50 (2013), pp. 124-130.

[4] I. Fedorova, F. Liu, F.B. Grumsen, Y. Cao, O.V. Mishin, and J. Hald, *Fine $(Cr, Fe)_2B$ borides on grain boundaries in a 10Cr-0.01B martensitic steel*, Scr. Mater. 156 (2018), pp. 124-128.

[5] Y. Gencer, *Influence of manganese on pack boriding behaviour of pure iron*, Surf. Eng. 27 (2011), pp. 634-638.

[6] A. Calik, Y. Gencer, M. Tarakci, K.O. Gunduz, and A.E. Gulec, *Boriding of equiatomic Fe-Mn binary alloy*, Acta Phys. Pol. A. 123 (2013), pp. 449-452.

[7] Y. Azakli, S. Cengiz, M. Tarakci, and Y. Gencer, *Characterisation of boride layer formed on Fe–Mo binary alloys*, Surf. Eng. 32 (2016), pp. 589-595.

[8] Y. Yi, J. Xing, X. Ren, H. Fu, Q. Li, and D. Yi, *Investigation on abrasive wear behaviour of Fe-B alloys containing various molybdenum contents*, Tribol. Int. 135 (2019), pp. 237-245.

[9] Y. Azakli, and M. Tarakci, *Microstructural characterisation of borided binary Fe–W alloys*, Surf. Eng. 34 (2016), pp. 226-234.

[10] Y. Azakli, K.O. Gunduz, M. Tarakci, and Y. Gencer, *A comparative study on boride layer morphology of Fe-4Co, Fe-4V and Fe-4W binary alloys*, Acta Phys. Pol. A. 127 (2015), pp. 1326-1330.

[11] K.O. Gunduz, Y. Gencer, M. Tarakci, and A. Calik, *The effect of vanadium on the boronizing properties of pure iron*, Surf. Coat. Technol. 221 (2013), pp. 104-110.

[12] Y. Gencer, M. Tarakci, and A. Calik, *Effect of titanium on the boronizing behaviour of pure iron*, Surf. Coat. Technol. 203 (2008), pp. 9-14.

[13] A. Meneses Amador, D. Sandoval Juarez, G.A. Rodriguez Castro, D. Fernandez Valdes, I. Campos Silva, R.C. Vega Moron, and J.L. Arciniega Martinez, *Contact fatigue performance of cobalt boride coating*, Surf. Coat. Technol. 353 (2018), pp. 346-354.

[14] R.Y. Lia, and Y.H. Duana, *Anisotropic elastic properties of MB (M = Cr, Mo, W) monoborides: a first-principles investigation*, Philos. Mag. 96 (2016), pp. 972-990.

[15] M. Kulka, N. Makuch, and M. Poplawski, *Two-stage gas boriding of Nisil in N_2–H_2–BCl_3 atmosphere*, Surf. Coat. Technol. 244 (2014), pp. 78–86.

[16] M. Kulka, *Current Trends in Boriding Techniques*, Springer Nature, Switzerland, 2019.

[17] M. Kulka, P. Dziarski, N. Makuch, A. Piasecki, and A. Miklaszewski, *Microstructure and properties of laser-borided Inconel 600-alloy*, Appl. Surf. Sci. 284 (2013), pp. 757–771.

[18] V. Sista, O. Kahvecioglu, G. Kartal, Q.Z. Zeng, J.H. Kim, O.L. Eryilmaz, and A. Erdemir, *Evaluation of electrochemical boriding of Inconel 600*, Surf. Coat. Technol. 215 (2013), pp. 452–459.

[19] S. Basturk, F. Senbabaoglu, C. Islam, M. Erten, I. Lazoglu, and T. Gulmez, *Titanium machining with new plasma boronized cutting tools*, Cirp Ann. Manuf. Techn. 59 (2010), pp. 101–104.

[20] A. Joshi, and S.S. Hosmani, *Pack-boronizing of AISI 4140 steel: boronizing mechanism and the role of container design*, Mater. Manuf. process. 29 (2014), pp. 1062–1072.

[21] I. Campos-Silva, M. Palomar-Pardave, R. Perez Pasten-Borja, O. Kahvecioglu Feridun, D. Bravo-Barcenas, C. Lopez-Garcia, and R. Reyes-Helguera, *Tribocorrosion and cytotoxicity of FeB-Fe_2B layers on AISI 316 L steel*, Surf. Coat. Technol. 349 (2018), pp. 986-997.

[22] I. Campos Silva, M. Ortiz Dominguez, M. Keddam, N. Lopez Perrusquia, A. Carmona Vargas, and M. Elias-Espinosa, *Kinetics of the formation of Fe_2B layers in gray cast iron: effects of boron concentration and boride incubation time*, Appl. Surf. Sci. 255 (2009), pp. 9290-9295.

[23] C.K.N. Oliveira, L.C. Casteletti, A. Lombardi Neto, G.E. Totten, and S.C. Heck, *Production and characterization of boride layers on AISI D2 tool steel*, Vacuum. 84 (2010), pp. 792–796.

[24] O. A. Gomez-Vargas, M. Keddam, and M. Ortiz-Dominguez, *Kinetics and tribological characterization of pack-borided AISI 1025 steel*, High. Temp. Mat. Proc. 36 (2017), pp. 197-208.

[25] B. Beausir, J. J. Fundenberger, *Analysis Tools for Electron and X-ray diffraction*, ATEX - software, www.atex-software.eu, Université de Lorraine - Metz, 2017.

[26] T. Nelis, and R. Payling, *Glow Discharge Optical Emission Spectroscopy: A Practical Guide*, Royal Society of Chemistry, Cambridge, 2003.

[27] J. Zhong, W. Qin, X. Wang, E. Medvedovski, J.A. Szpunar, and K. Guan, *Mechanism of texture formation in iron boride coatings on low-carbon steel*, Metall. Mater. Trans. A. 50 (2019), pp. 58-62.

[28] M. Kulka, N. Makuch, and A. Piasecki, *Nanomechanical characterization and fracture toughness of FeB and Fe_2B iron borides produced by gas boriding of Armco iron,* Surf. Coat. Technol. 325 (2017), pp. 515-532.

[29] C.M. Brakman, A.W.J. Gommers, and E.J. Mittemeijer, *Boriding of Fe and Fe–C, Fe–Cr, and Fe–Ni alloys; Boride-layer growth kinetics,* J. Mater. Res. 4 (1989), pp. 1354-1370.

[30] M. Keddam, R. Chegroune, M. Kulka, D. Panfil, P. Siwak, and S. Taktak, *Characterization, tribological and mechanical properties of plasma paste borided AISI 316 steel*, Trans. Indian Inst. Met. 71 (2018), pp. 79-90.

[31] L.C. Casteletti, A.N. Lombardi, G.E. Totten, Boriding. In: Wang Q.J., Chung YW. (eds) *Encyclopedia of Tribology*, Springer, Boston, MA, 2013.

[32] Y. Duan, P. Li, Z. Chen, J. Shi, and L. Ma, *Surface evolution and growth kinetics of Ti6Al4V alloy in pack boriding*, J. Alloys Compd. 742 (2018), pp. 690-701.

[33] S.S. Hosmani, R.E. Schacherl, and E.J. Mittemeijer, *Kinetics of nitriding Fe-2 Wt Pct V alloy: mobile and immobile excess nitrogen*, Metall. Mater. Trans. A. 38 (2007), pp. 7-16.

[34] R.E. Schacherl, P.C.J. Graat, and E.J. Mittemeijer, *The nitriding kinetics of iron-chromium alloys; the role of excess nitrogen*, Metall. Mater. Trans. A. 35 (2004), pp. 3387-3398.

[35] V. Jain, and G. Sundararajan, *Influence of the pack thickness of the boronizing mixture on the boriding of steel*, Surf. Coat. Technol. 149 (2002), pp. 21-26.

[36] A.M. Gatey, S.S. Hosmani, C.A. Figueroa, S.B. Arya, and R.P. Singh, *Role of surface mechanical attrition treatment and chemical etching on plasma nitriding behavior of AISI 304L steel*, Surf. Coat. Technol. 304 (2016), pp. 413-424.

[37] S.S. Hosmani, R.E. Schacherl, and E.J. Mittemeijer, *Nitrogen uptake by a Fe-V alloy: Quantitative analysis of excess nitrogen*, Acta Mater. 54 (2006), pp. 2783-2792.

[38] I. Campos Silva, M. Dominguez, N. Lopez-Perrusquia, A. Meneses-Amador, R. Escobar-Galindo, and J. Martınez-Trinidad, *Characterization of AISI 4140 borided steel*, Appl. Surf. Sci. 256 (2010), pp. 2372–2379.

List of the figure captions

Figure 1: XRD patterns recorded from the surface of the non-treated and boronized specimens.

Figure 2: (a) Optical and (b) SEM micrographs in the cross-section of the specimen boronized at 950°C for 4 h. (c) Microhardness-depth profiles for the specimens boronized at 850, 950 and 1050°C for 4 h.

Figure 3: (a) SEM, (b) IPF, (c)-(d) phase maps and, (e) Pole figures of the specimen boronized at 1050°C for 4 h. White spots in (c) indicate unindexed areas.

Figure 4: (a) BSE micrograph of specimen boronized at 950°C for 4 h. (b) Elemental concentration-depth profiles by EPMA from the surface to the non-boronized region, as shown in (a).

Figure 5: Distribution of vital elements in the cross-section of the specimen boronized at 950°C for 4 h) shown in (a) as BSE micrograph and (b) B, (c) Fe, (d) Al, (e) Cr and (f) Mo as chemical mappings. The colored scale bars at the right show relative concentration of the elements (low (bottom) to high (top)).

Figure 6: GDOES concentration-depth profiles of the elements in the surface layer for the specimens boronized (a) at 950°C for 4 h and (b) at 850°C for 4 h.

Figure 7: Variation in the slope of the GDOES concentration-depth profiles (shown in Fig. 6) of boron and alloying elements present in the surface layer of the specimens boronized at (a) 950°C for 4 h and (b) 850°C for 4 h.

Figure 8: (a) GDOES concentration-depth profiles of boron and (b) corresponding slope variations in the surface layer for the specimens boronized at 850, 950, and 1050°C for 4 h.

Figure 9: Micrographs in the cross-sections of the boronized specimens. Arrows indicate some of the boride particles formed at grain-boundaries in the transition zone.

Figure 10: GDOES concentration-depth profiles of the elements in the surface layer for the specimens boronized at 950°C for 2, 4, and 6 h.

Figure 11: Variation in the slope of the GDOES concentration-depth profiles (shown in Fig. 10) of the elements in the surface layer for the specimens boronized at 950°C for 2, 4, and 6 h.

Figure 12: (a) Depths corresponding to p1 and p2 (shown in Fig. 11) for the elements present in the specimens boronized at 950°C for 2, 4, and 6 h. (b) Magnified view of the B and Ni profiles near to the non-boronized core of the specimen boronized at 950°C for 4 h. (c) Rates determined using the data shown in (a) for the elements present in the steel.

Figure 13: Schematic presentation of the boronizing mechanism: (a)-(e) Steps in the development of microstructure and elemental profiles. Positions of the elemental profiles (concerning each other) are arbitrary.

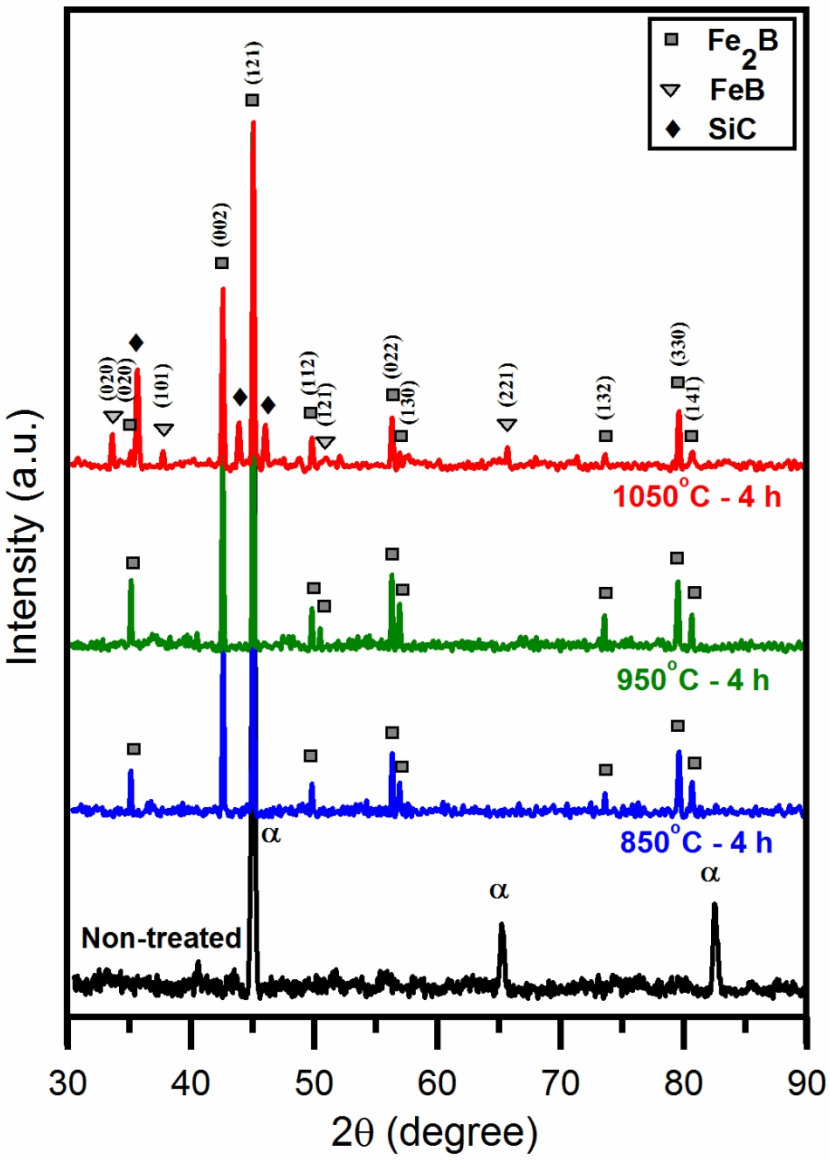

Figure 1: XRD patterns recorded from the surface of the non-treated and boronized specimens.

88x127mm (300 x 300 DPI)

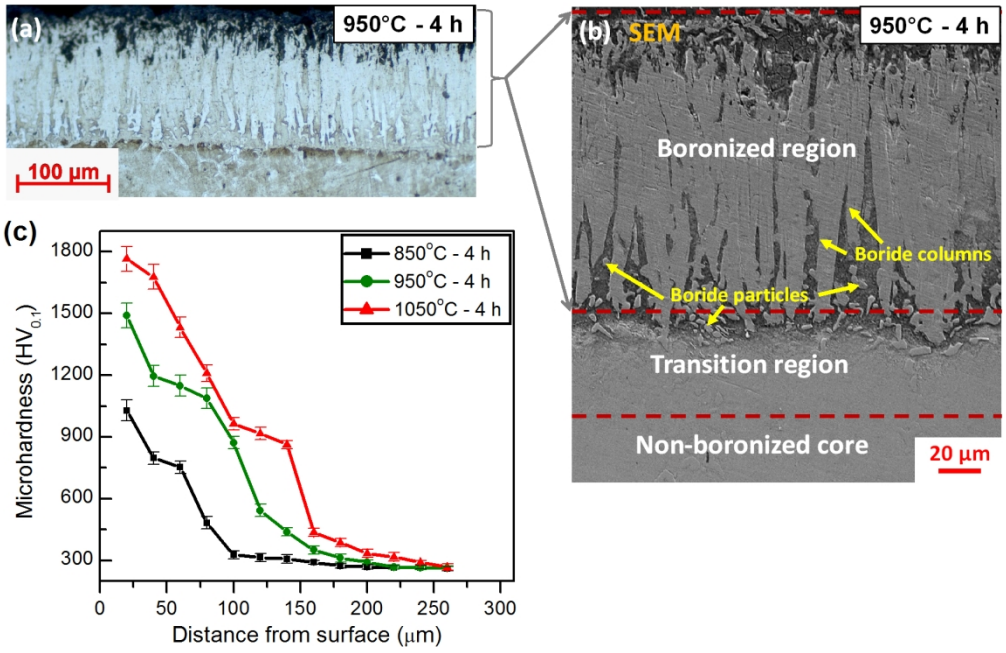

Figure 2: (a) Optical and (b) SEM micrographs in the cross-section of the specimen boronized at 950°C for 4 h. (c) Microhardness-depth profiles for the specimens boronized at 850, 950 and 1050°C for 4 h.

314x203mm (150 x 150 DPI)

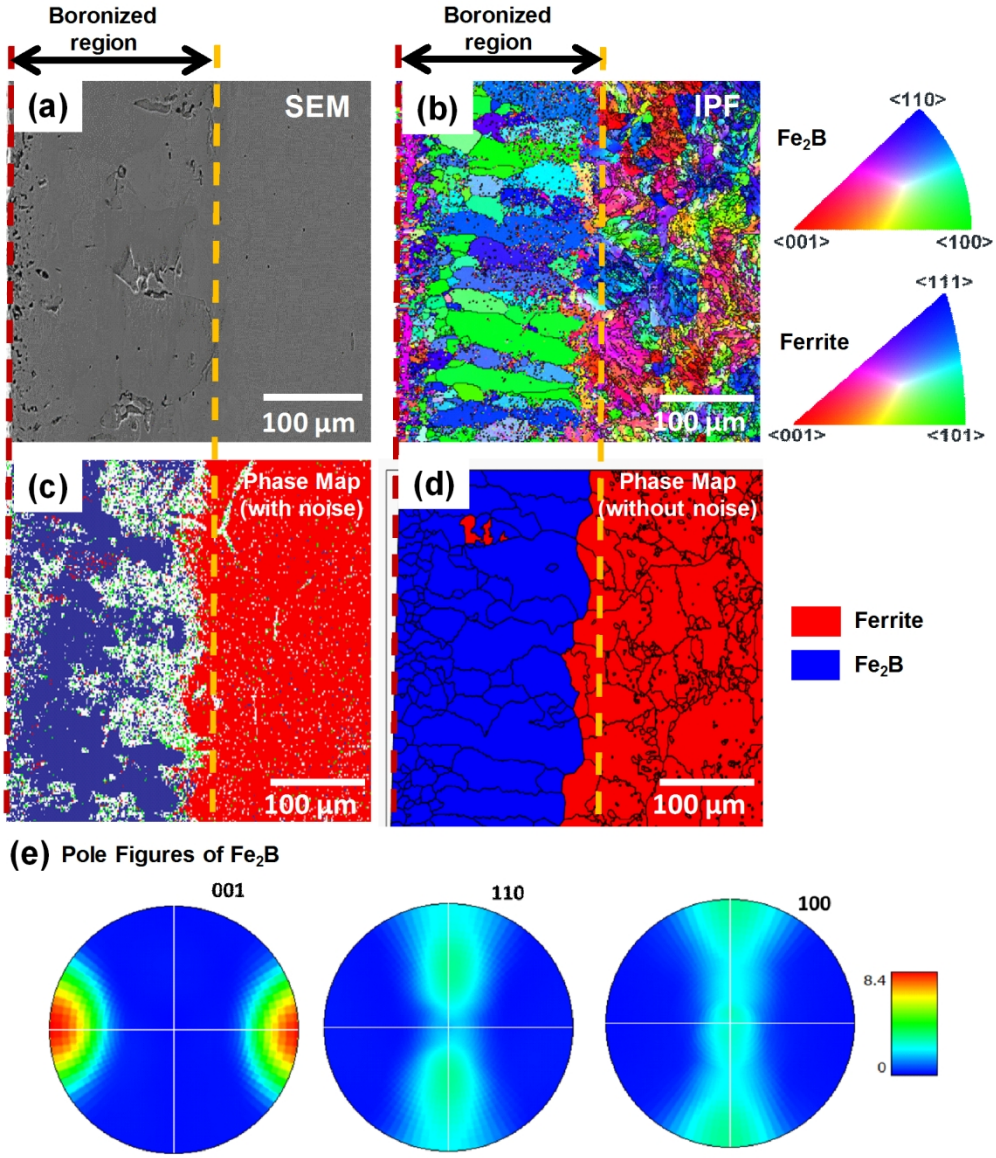

Figure 3: (a) SEM, (b) IPF, (c)-(d) phase maps and, (e) Pole figures of the specimen boronized at 1050°C for 4 h. White spots in (c) indicate unindexed areas.

314x365mm (150 x 150 DPI)

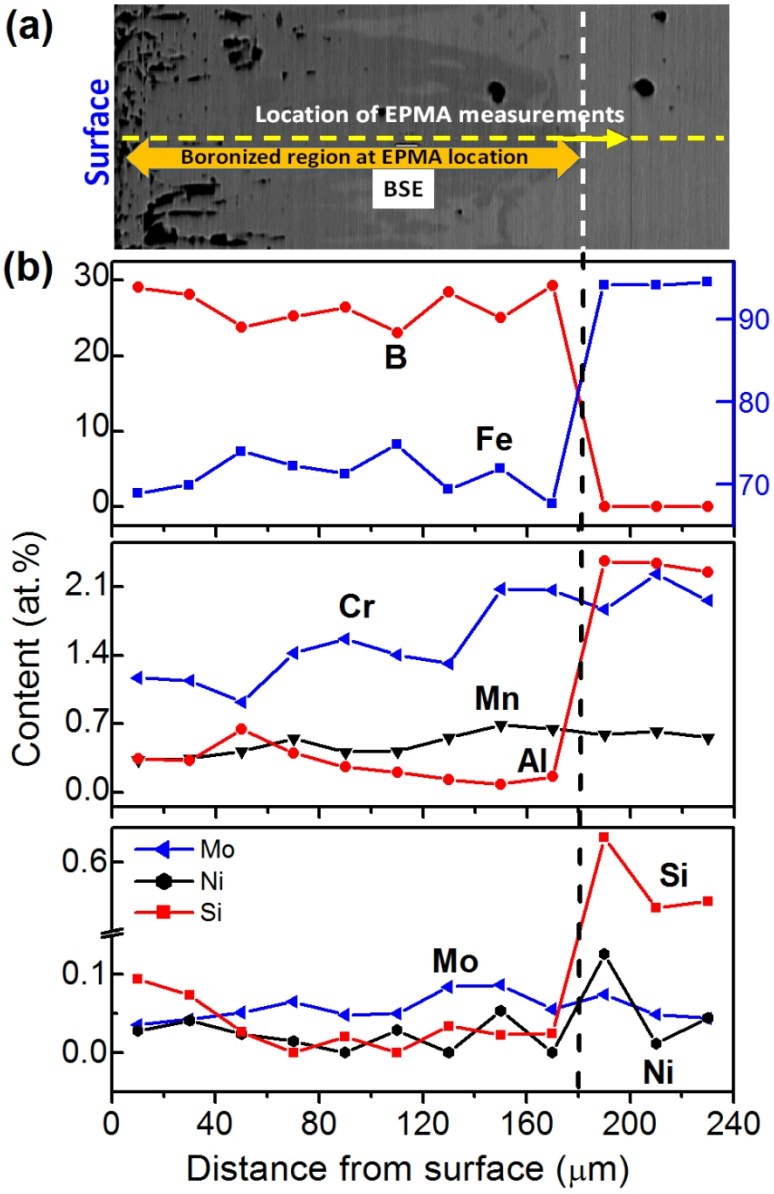

Figure 4: (a) BSE micrograph of specimen boronized at 950°C for 4 h. (b) Elemental concentration-depth profiles by EPMA from the surface to the non-boronized region, as shown in (a).

162x254mm (150 x 150 DPI)

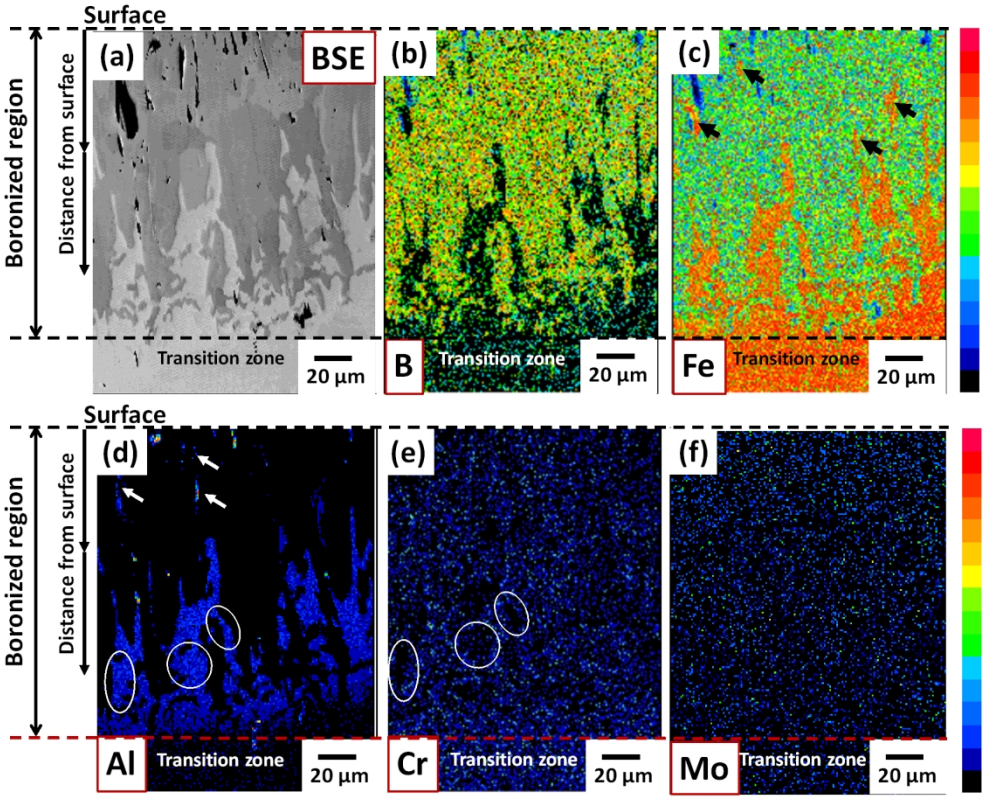

Figure 5: Distribution of vital elements in the cross-section of the specimen boronized at 950°C for 4 h) shown in (a) as BSE micrograph and (b) B, (c) Fe, (d) Al, (e) Cr and (f) Mo as chemical mappings. The colored scale bars at the right show relative concentration of the elements (low (bottom) to high (top)).

314x254mm (150 x 150 DPI)

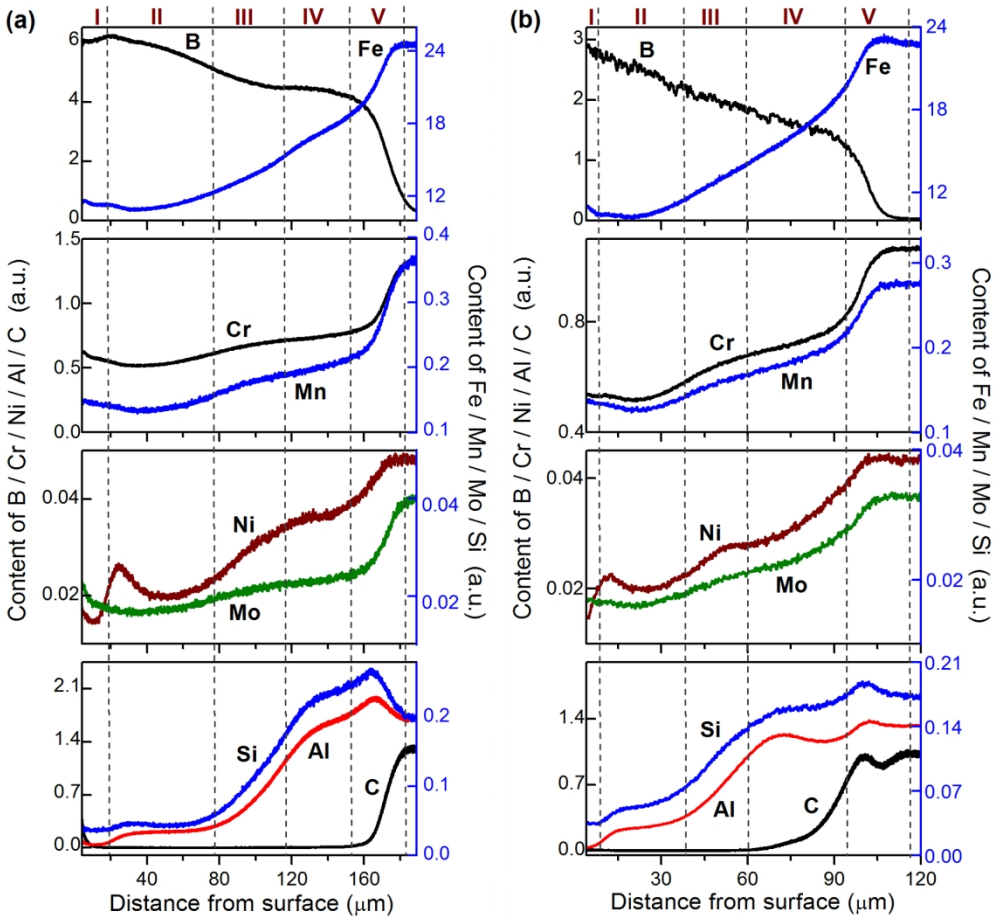

Figure 6: GDOES concentration-depth profiles of the elements in the surface layer for the specimens boronized (a) at 950°C for 4 h and (b) at 850°C for 4 h.

314x289mm (150 x 150 DPI)

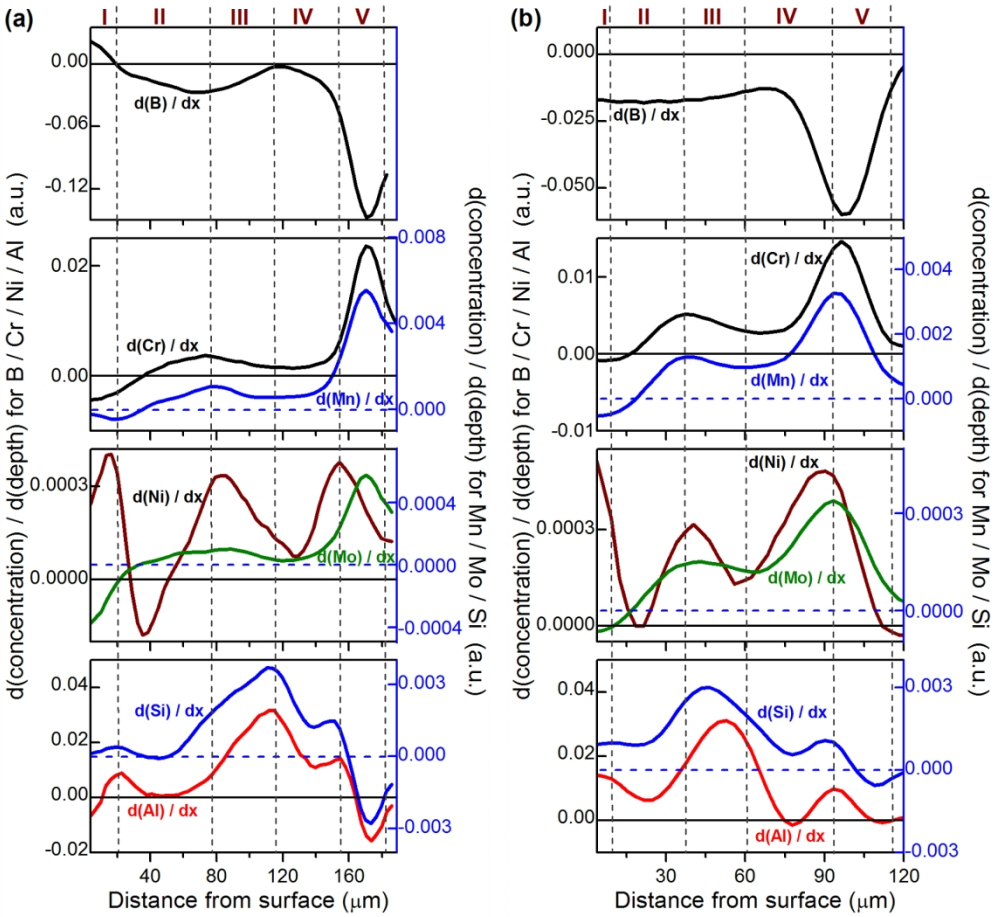

Figure 7: Variation in the slope of the GDOES concentration-depth profiles (shown in Fig. 6) of boron and alloying elements present in the surface layer of the specimens boronized at (a) 950°C for 4 h and (b) 850°C for 4 h.

314x289mm (150 x 150 DPI)

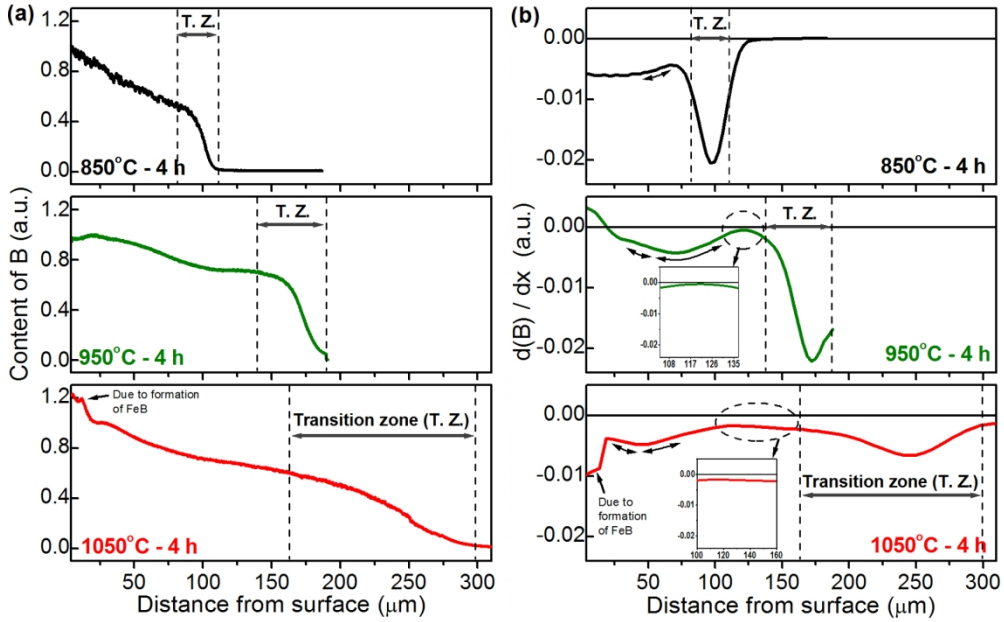

Figure 8: (a) GDOES concentration-depth profiles of boron and (b) corresponding slope variations in the surface layer for the specimens boronized at 850, 950, and 1050°C for 4 h.

314x198mm (150 x 150 DPI)

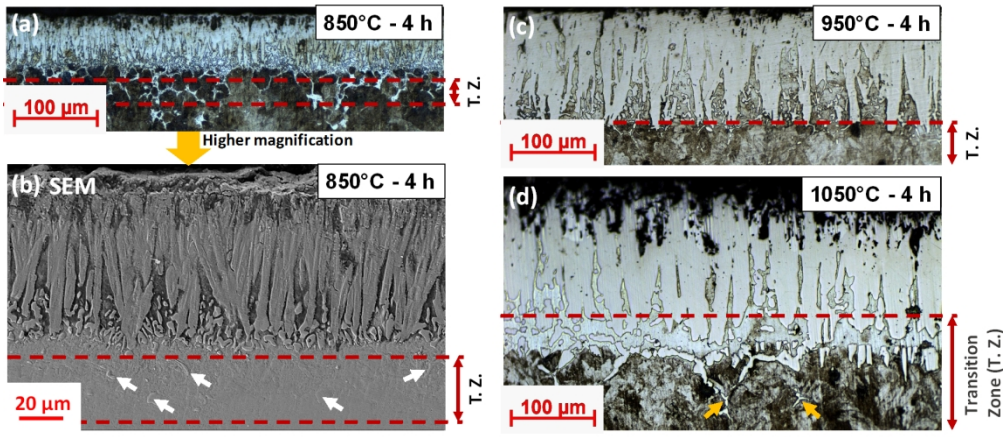

Figure 9: Micrographs in the cross-sections of the boronized specimens. Arrows indicate some of the boride particles formed at grain-boundaries in the transition zone.

314x142mm (150 x 150 DPI)

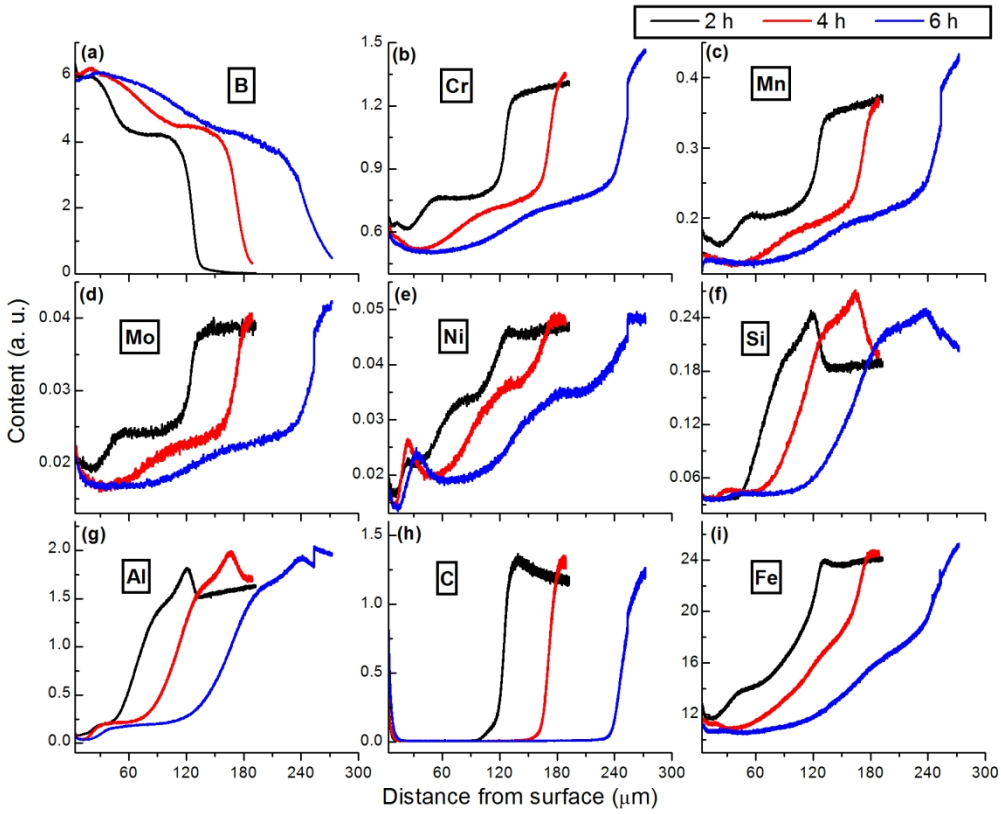

Figure 10: GDOES concentration-depth profiles of the elements in the surface layer for the specimens boronized at 950°C for 2, 4, and 6 h.

314x254mm (150 x 150 DPI)

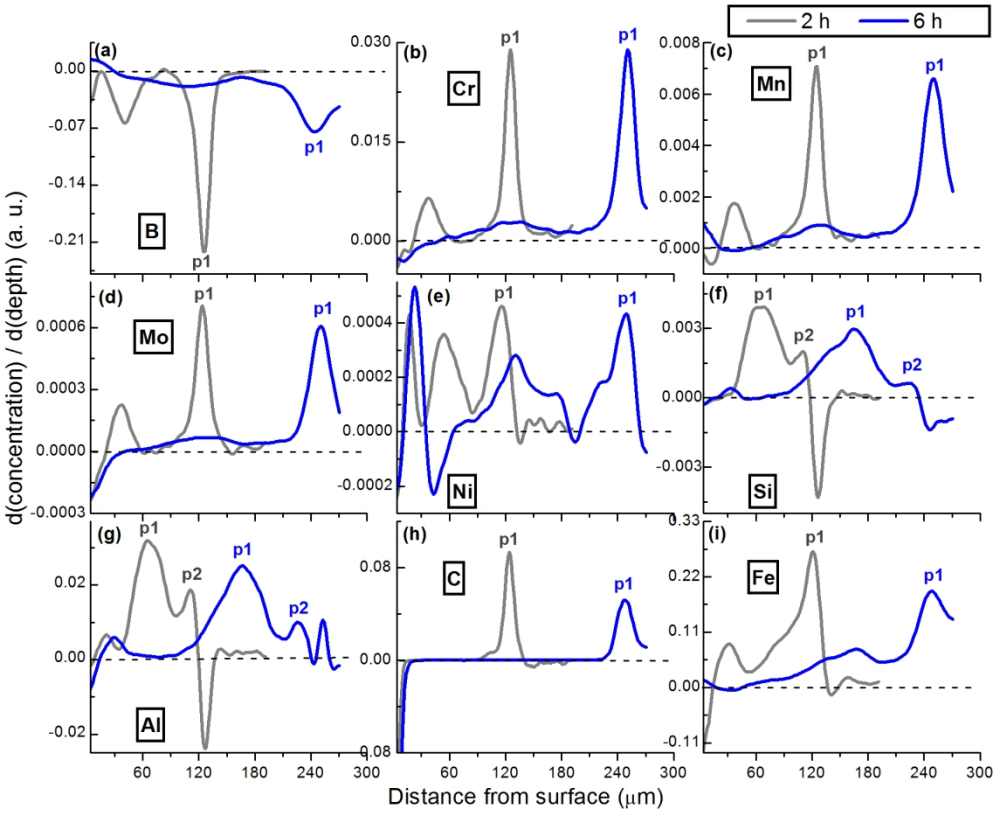

Figure 11: Variation in the slope of the GDOES concentration-depth profiles (shown in Fig. 10) of the elements in the surface layer for the specimens boronized at 950°C for 2, 4, and 6 h.

314x254mm (150 x 150 DPI)

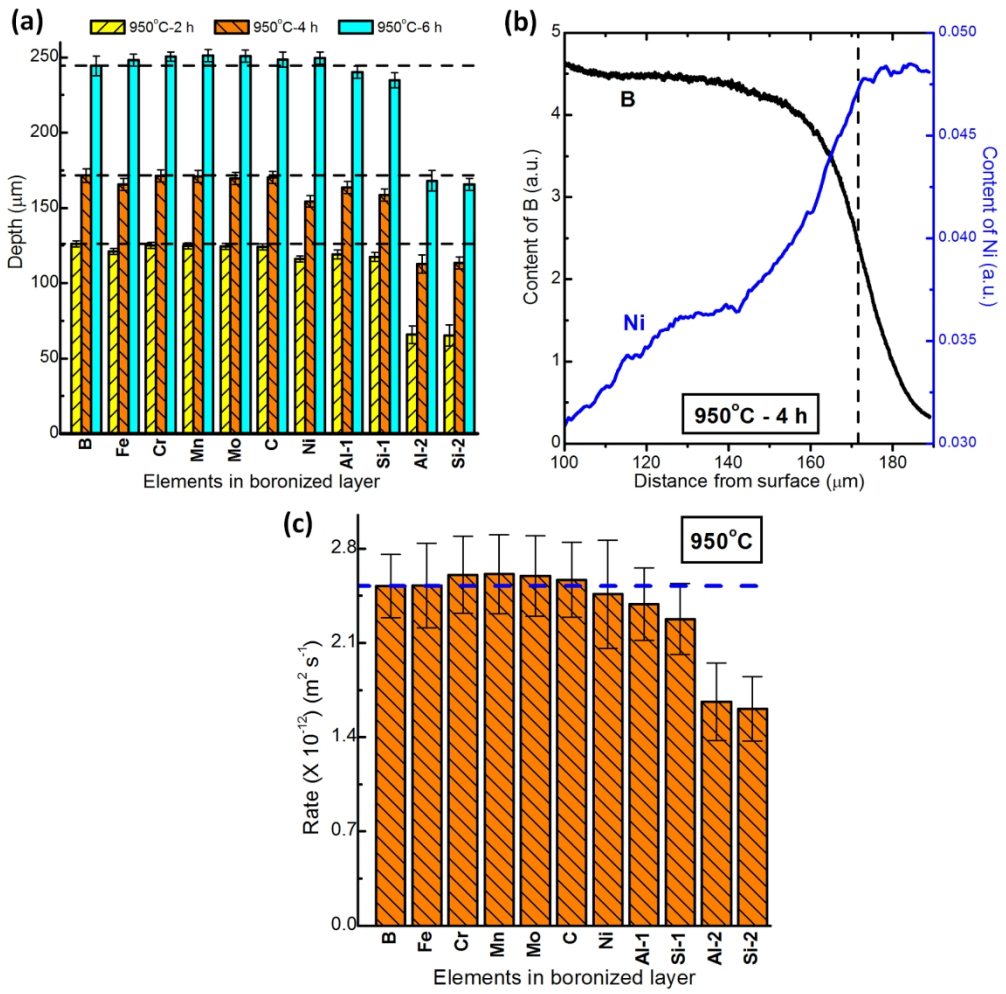

Figure 12: (a) Depths corresponding to p1 and p2 (shown in Fig. 11) for the elements present in the specimens boronized at 950°C for 2, 4, and 6 h. (b) Magnified view of the B and Ni profiles near to the non-boronized core of the specimen boronized at 950°C for 4 h. (c) Rates determined using the data shown in (a) for the elements present in the steel.

314x314mm (150 x 150 DPI)

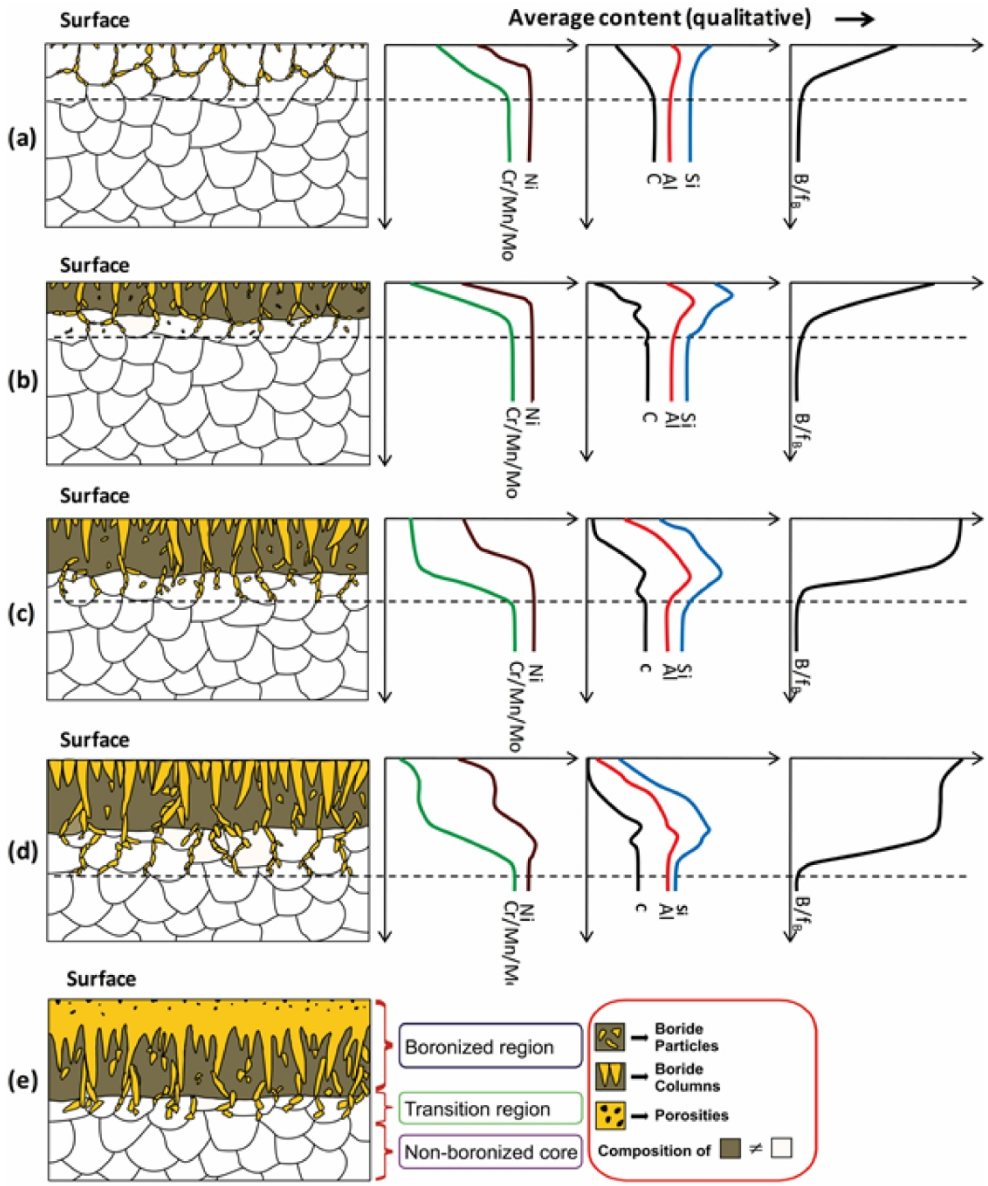

Figure 13: Schematic presentation of the boronizing mechanism: (a)-(e) Steps in the development of microstructure and elemental profiles. Positions of the elemental profiles (concerning each other) are arbitrary.

629x767mm (150 x 150 DPI)